Chemical Geology 449 (2017) 123–134

Contents lists available at ScienceDirect

Chemical Geology

journal homepage: www.elsevier.com/locate/chemgeo

Siderite dissolution coupled to iron oxyhydroxide precipitation in the presence of arsenic revealed by nanoscale imaging

François Renard [a,b,*], Christine V. Putnis [c,d], German Montes-Hernandez [b], Helen E. King [e]

[a] Department of Geosciences, Physics of Geological Processes, University of Oslo, Norway
[b] University Grenoble Alpes, CNRS, ISTerre, CS 40700, F-38058 Grenoble Cedex 9, France
[c] Institut für Mineralogie, University of Münster, Corrensstrasse 24, 48149 Münster, Germany
[d] The Institute for Geoscience Research (TIGeR), Department of Chemistry, Curtin University, Perth 6845, Australia
[e] Department of Earth Sciences, Utrecht University, Budapestlaan 4, 3584 CD Utrecht, The Netherlands

ARTICLE INFO

Article history:
Received 25 September 2016
Received in revised form 29 November 2016
Accepted 1 December 2016
Available online 3 December 2016

Keywords:
Siderite
Iron oxyhydroxide
Arsenic
Atomic force microscopy

ABSTRACT

Siderite, the iron carbonate mineral, occurs in several geological environments and contributes to both the global iron and CO_2 cycles. Under crustal conditions, this mineral may dissolve, releasing iron that becomes oxidized and then precipitates in the form of iron oxides and oxyhydroxides that have a high affinity for pollutants, such as arsenic. The process of siderite dissolution, dissolved iron oxidation, and oxyhydroxide precipitation is coupled in time and space. Here, we study the entire process using time-lapse in-situ atomic force microscopy. Natural siderite crystals were dissolved at room temperature in acidic aqueous solutions in the presence or absence of arsenic. The dissolution process, whose rate could be measured at a nanometer scale, occurred by the nucleation and growth of etch pits, the retreat of step edges, and the deepening of cleavage steps. Precipitation of iron oxyhydroxide phases coupled to siderite dissolution was imaged in-situ. Nucleated particles have an initial height of 1–2 nm after 1 minute reaction and then grow with time into aggregate precipitates 130–220 nm wide and up to 80 nm high after 24 h of reaction. Ex-situ stirred-flow reactor measurements confirm the same sequence of siderite dissolution and iron oxyhydroxide precipitation. The arsenic is adsorbed by iron oxyhydroxides and its presence does not change significantly the rate of dissolution-precipitation of the overall process. Results provide a basis for understanding and quantifying the interactions between reduced-iron minerals and aqueous-phase oxidants, as well as potential sequestration of toxic elements such as arsenic.

1. Introduction

Carbonates are common minerals in the Earth's upper crust and because of their high reactivity they dissolve and precipitate easily, thus playing a key role in the global cycle of carbon, controlling the weathering of continents and controlling the composition of groundwaters through pH, alkalinity or metal concentrations. Siderite, $FeCO_3$, is a trigonal carbonate mineral found in several geological environments, where it forms under reducing conditions providing sufficient iron in the 2+ oxidation state to build the mineral. It often occurs as a carbonate solid solution, with substitutions of the iron ion with Mg^{2+}, Mn^{2+}, Zn^{2+}, and a limited solid solution with Ca^{2+} (as a result of the ionic radii differences). It is also an end-product of bacterial anaerobic activity. In the presence of oxygen, Fe^{2+} from siderite is oxidized and thereafter participates in the global iron cycle through various $Fe^{(III)}$-rich oxides and oxyhydroxides.

1.1. Siderite in geological environments

Several studies show that siderite precipitates at shallow conditions and sometimes at depth during diagenesis (Morad et al., 1994; Milliken, 1998; Rossi et al., 2001; Stel, 2009). In some geological environments it is also found associated with the presence of arsenic. In all cases, siderite precipitation history is complex with successive events of siderite precipitation and dissolution largely controlled by the redox conditions. Rossi et al. (2001) described widespread siderite precipitation in sandstone reservoirs in the Khatatba formation in Egypt. There, siderite cements quartz grains and has produced a matrix strong enough such that compaction was reduced and porosity was preserved. Later dissolution of the siderite created a secondary porosity, enhancing reservoir properties of the rock. The siderite was assumed to have precipitated in shallow conditions, for example below swamps, where reducing conditions allowed the presence of Fe^{2+} in the pore water.

Carbonate cemented red-bed arkose deposits in the Central Iberian Chain (Spain) show that siderite participated in the formation and destruction of porosity during diagenesis (Stel, 2009). In this example, reduction of iron oxides and the dissolution of calcite were followed by a

* Corresponding author at: Department of Geosciences, PGP, University of Oslo, Box 1048, 0316 Blindern, Oslo, Norway.
E-mail address: francois.renard@geo.uio.no (F. Renard).

http://dx.doi.org/10.1016/j.chemgeo.2016.12.001
0009-2541/

deformation episode during which the reducing fluid percolated along a nearby fault and caused siderite precipitation. These reactions are associated with a volume loss close to 50% resulting in secondary porosity.

Siderite limits iron aqueous concentration in geological environments and also its bioavailability in soils and river and lake sediments. In acid mine drainage environments, it represents a key component in the suite of mineral reactions that occur during reactive transport in groundwaters (Walter et al., 1994). As Fe^{2+} is produced by the dissolution of sulfide minerals, siderite can precipitate if limestone or dolomite dissolves nearby, saturating the fluid with carbonate so that supersaturation with respect to siderite is reached. Numerical modelling shows that once calcite is completely dissolved, siderite will also dissolve, releasing Fe^{2+} to the fluid that can become oxidized and precipitate in the form of iron oxides and oxyhydroxides, such as goethite (Walter et al., 1994). In the numerical simulations performed by these authors, a front of siderite precipitates and then dissolves, moving with time in the same direction as the flow of acid mine drainage.

In the Appalachian region, iron-contaminated groundwater leaks along abandoned and unplugged oil and gas wells where siderite is the main source of iron into the water (Hedin et al., 2005; Chapman et al., 2013). Strontium isotopes indicate that the enrichment in iron is due to the downward percolation of acid water coming from surface spoils of coal mine products through a siderite-rich shallow sandstone layer (Chapman et al., 2013), and then its upward circulation along fluid pathways such as fractures and abandoned wells. Here, the mechanism proposed is similar to that of acid mine drainage, where the siderite is the source of iron instead of sulfide minerals. Siderite was also found in West Bengal sediments, where arsenic contamination of groundwater is a major health issue (Pal et al., 2002). Finally, the spatial correlation of arsenic release and siderite dissolution was also observed at a local scale in the groundwater contaminated by arsenic in the ChaiNan floodplain, Taiwan (Lin et al., 2006). As proposed in the present study, a possible explanation of this observation is that arsenic is adsorbed on iron oxyhydroxides that cover the siderite surfaces and is then released during siderite dissolution because of pH variations.

1.2. Using siderite to remediate polluted waters

Siderite could be used in environmental technologies that remediate acid discharge pollution, and several field and laboratory studies have provided data that characterize the coupled processes involved. Processing the discharge of acidic effluents using reactive barriers is a technology used to reduce the environmental impacts of acid mine drainage. The precipitation of siderite is one of the many reactions that can buffer fluid pH and decrease iron concentration, as observed in a field experiment near the Nickel Rim mine in Ontario (Benner et al., 1999). In the case of soil contamination by arsenic, for example where As_2O_3 has been applied as a herbicide, the use of siderite with an oxidizing agent could produce oxyhydroxides and trap arsenic.

In laboratory conditions, a siderite/limestone reactor was proposed to trap arsenic and cadmium from polluted water (Wang and Reardon, 2001). Fluids with high concentrations of iron, cadmium, and arsenic were acidified with dissolved carbon dioxide and injected into a reactor made of two successive columns. The first column contained siderite, which dissolved, released Fe^{2+} that oxidized into Fe^{3+} and formed iron oxyhydroxides that could trap arsenic. Then, the fluid was transported into a second column that contained calcium carbonate where cadmium was trapped by the precipitation of calcium and cadmium carbonates. After some time the efficiency of the first reactor was reduced and this was interpreted by an armoring effect of iron oxyhydroxide coatings on siderite grains.

Guo et al. (2007a,b) developed a water filtering technique that uses siderite as a natural adsorbent of arsenic. In these studies, either 0.1–0.25 mm size siderite grains or mixture of quartz, siderite, and hematite grains were reacted with arsenic contaminated water at concentrations in the range 0.2–1 ppm. Both $As^{(V)}$ and $As^{(III)}$ were successfully adsorbed. The proposed mechanism was an initial adsorption of arsenic on the siderite grains, and then the formation of iron oxyhydroxides (goethite or ferrihydrite) on which arsenic was later adsorbed or sequestered. Electron microscope images showed the formation of a 300 nm thick layer of iron oxides at the surface of the siderite grains (Guo et al., 2007a). Using X-ray photoelectron spectroscopy, it was confirmed that an iron hydroxide layer precipitated at the surface of siderite (Tang and Martin, 2011). All these studies show that dissolution of siderite and iron oxyhydroxide precipitation are coupled, and that iron oxyhydroxides can be used to sequester pollutants, such as arsenic.

Here, we perform in-situ time-resolved nanoscale imaging of the coupled process to document 1) the detailed mechanisms of siderite dissolution at low pH, in the range 1–5.5 and compare it with bulk dissolution experiments, 2) the precipitation rate and morphology of iron oxyhydroxide particles and how they nucleate and grow on the siderite surface, and 3) the possibility that arsenic is adsorbed during this process. The choice of low pH conditions in the range 1–5 is relevant for several environments such as leakage from oil and gas boreholes or acid mine drainage where arsenic and iron oxyhydroxides are observed (Benner et al., 1999; España et al., 2007) or even more extreme fluids with extremely low pH, as observed in an underground mine in California (Nordstrom et al., 2000). Our results complement previous studies where siderite dissolution was either measured in batch reactors (Golubev et al., 2009) or imaged using atomic force microscopy (Duckworth and Martin, 2004; Tang and Martin, 2011) and where adsorption of arsenic on iron oxyhydroxide was characterized (Dixit and Hering, 2003). These previous studies were limited in observing directly processes and measuring quantitative information on the rates of dissolution and precipitation at the nanoscale. Here, we observe that siderite dissolution occurs by three mechanisms at the atomic scale: etch pits nucleation and spreading, step edge retreat, and widening and deepening of cleavage planes. The present study also provides constraints on the mechanism of growth of the iron oxyhydroxide particles and, for the first time, measure their size (height and width) as a function of time. Because dissolution of siderite is coupled to precipitation of iron oxyhydroxide, the whole process must occur in a boundary layer at the siderite surface.

2. Materials and methods

2.1. Siderite crystals

A siderite crystal (Einigkeit Mine, Neunkirchen, Siegerland, Germany) was obtained from the mineral collection of the University of Münster. Inductively coupled plasma - optical emission spectroscopy (ICP-OES) revealed the composition of the crystal, with Mn (656 ppm or 6.86 wt.%) and only trace amounts of Ca (46 ppm), Mg (147 ppm), Zn (421 ppb) and Sr (26 ppb) detected. Fresh siderite fragments (ca. $4 \times 2 \times 1$ mm) were prepared directly before each experiment from this single siderite crystal by cleaving the crystal parallel to the {10–14} plane. Several fragments were also crushed into powder for stirred flow-through reactor experiments.

2.2. Solutions for siderite dissolution under the atomic force microscope

Arsenic-free solutions and solutions with a controlled amount of arsenic ($As^{(III)}$ or $As^{(V)}$), with the same ionic strength and various pH values, were used for siderite dissolution experiments (Table 1). Several solutions with identical compositions were used to test the reproducibility of the obtained results. Firstly, arsenic-free aqueous solutions with controlled pH, between 1.6 and 5.5, and ionic strength equal to 0.047 M were injected into a flow-through fluid cell of an atomic force microscope (AFM) to dissolve the siderite surface. These solutions were prepared using doubled deionized water (resistivity > 18 mΩ·cm) directly before each experiment. Sodium chloride and hydrochloric acid were used to adjust ionic strength and pH, respectively. The pH and salinity were

Table 1
List of in-situ atomic force microscope (AFM) and stirred flow-through reactor experimental conditions for coupled siderite dissolution and iron oxyhydroxide precipitation in the presence of arsenic. The pH is that of the injected solution.

Exp. #	Ionic strength (mole/L)	Duration (hour)	Arsenic concentration	pH measured	Precipitates (surface area covered)
AFM					
sid01	0.047	5.2	0	5.5	
			$As^{(V)}$, 50 ppm	1.3	<5%
			$As^{(V)}$, 500 ppm	1.6	<5%
sid02	0.047	21.9	$As^{(V)}$, 500 ppm	1.6	>80%
sid03	0.047	3.5	0	5.5	
			$As^{(V)}$, 50 ppm	1.3	<5%
			$As^{(V)}$, 500 ppm	1.6	<5%
sid04	0.047	24	0	5.5	
			$As^{(V)}$, 500 ppm	4.7	>80%
sid05	0.047	21	0	5.5	
			$As^{(III)}$, 500 ppm	4.7	>80%
sid06	0.047	28.5	0	5.5	
			$As^{(III)}$, 500 ppm	1.6	<10%
sid07	0.047	2.2	0	5.4	
			$As^{(V)}$, 500 ppm	2.8	no precipitates after 2 h
sid08	0.047	24.9	0	5.5	
			$As^{(V)}$, 500 ppm	1.7	<5%
sid09	0.047	23.5	0	5.5	
			$As^{(V)}$, 500 ppm	2.1	>80%
sid10	0.047	24	0	5.5	<20%, precipitates aligned along steps
sid11	0.047	17	0	1.6	>80%
sid12	0.047	17	0	2.8	<10%
sid13	0.047	1.2	$As^{(III)}$, 500 ppm	11.7	no precipitates
sid14	0.047	1	$As^{(V)}$, 500 ppm	12.1	no precipitates
sid15	0.047	8.7	0	2	<10%
				1	>80%
sid16	0.047	0.8	0	2	<10%
				1	>80%
Reactor					
Ba1	0.047	2.3	$As^{(III)}$, 500 ppm	5	–
Ba2	0.047	2.3	$As^{(V)}$, 500 ppm	2	–

adjusted according to thermodynamic simulations of equilibrated solutions using the PHREEQC software (Parkhurst and Appelo, 1999). Then, solutions with $As^{(III)}$ or $As^{(V)}$ oxyanions at concentrations of 50 or 500 ppm, with the same ionic strength as the arsenic-free aqueous solutions initially used, were injected into the fluid cell, under several pH conditions (Table 1). The arsenic solutions were prepared from salts of sodium arsenite ($NaAsO_2$) and sodium arsenate dibasic heptahydrate ($Na_2HAsO_4 \cdot 7H_2O$) dissolved into double deionized water. The pH of the solutions was controlled to be similar in the presence and in the absence of arsenic. As well, the pH of all solutions was measured independently using a pH-meter confirming the PHREEQC simulation results. All chemical agents were obtained from Sigma Aldrich®.

2.3. Atomic force microscopy imaging

The siderite surfaces were scanned at room temperature (23 ± 1 °C) using a Bruker Multimode atomic force microscope (AFM) operating in contact mode. All time-resolved sequences were acquired downscan. The experiments were performed in-situ within an O-ring sealed flow-through fluid cell from Digital Instruments (Bruker). Volumes of 2 mL of solutions were injected with a syringe between each scan, at regular time intervals of approximately 1.5 min, giving an effective flow rate of 22 $\mu L \cdot s^{-1}$. This flow rate ensures that processes occurring at the mineral surface are reaction-controlled, rather than diffusion controlled (Ruiz-Agudo et al., 2010).

AFM images were collected using Si_3N_4 tips (Veeco Instruments, tip model NP-S20) with spring constants 0.12 N m^{-1} and 0.58 N m^{-1}. Images were analyzed using the NanoScope Analysis software (Version 1.5). At the beginning of each dissolution experiment, deionized water was injected over the siderite surface for several minutes, to observe any reaction or dissolution. For several samples, the dissolution was followed under the AFM for several hours, then the sample was removed from the flow cell, left in contact with the solution for 12 to 20 h, and then imaged again, to allow sufficient time for reaction.

2.4. Ex-situ dissolution experiments

Ex-situ siderite dissolution stirred flow-through reactor experiments were performed to determine if arsenic is adsorbed on siderite. Two flow-through reactors of 50 mL (internal volume) were firstly filled with high-purity water, one reactor containing 1 g of natural siderite ground in a McCrone micronizer agate mortar in ethanol for 8 min (particle size < 30 μm). The other reactor did not contain siderite and was used passively to trace the fluid and show that no adsorption occurred on the walls. Then, an arsenic-rich solution (100 to 500 mg/L of $As^{(III)}$ at pH = 5 or 100 to 500 mg/L of $As^{(V)}$ at pH = 2) was percolated in both reactors using a constant flow rate of 3.3 mL/min. The siderite-solution suspension in the reactor was continuously stirred by a magnetic Teflon bar at room temperature (20 °C). The outflow solutions were filtered in-situ through 0.2 μm pore size Teflon membranes (located on the top of reactors) and pH and ICP-AES (inductively coupled plasma - atomic emission spectroscopy) analyses were taken on-line. Thereby iron and arsenic concentrations were measured as a function of time allowing to detect i) if iron is released in the fluid, ii) if arsenic is adsorbed onto siderite or the produced iron oxyhydroxides.

2.5. Raman spectroscopy

A confocal Raman spectrometer (WITec Alpha 300R) operating with the 532 nm line of a Nd-YAG laser was used for analysis of reaction products. Samples with large numbers of precipitates observed in the AFM experiments and the powders from the reactor experiments were selected for Raman investigations. The original siderite was also analyzed as a reference. To survey samples for newly precipitated material, different areas of the sample surface with visual precipitates were scanned using the continuous scan mode with an integration time of 0.2 s. A filter averaged over 2 × 2 pixels was used to identify areas of the spectra where additional, weaker peaks unrelated to the underlying siderite were present. Once an area with additional peaks was detected a depth scan was used with the same parameters as the continuous scan to determine the best focal point. Finally, a single spectrum with improved signal to noise ratio was obtained using an integration time of 5 s and integrated 50 times. All spectra were obtained using a grating of 1800 grooves/mm and a pinhole of 20 μm. Spectral background removal and peak fitting was conducted using the WITec Project Plus software.

3. Results

3.1. In-situ atomic force microscope experiments

The siderite cleaved surface is characterized by the presence of steps (Fig. 1a). Direct in situ observations showed that in contact with acidic solutions, the siderite surface starts dissolving along steps that retreat, through the formation and propagation of etch pits with typical rhombohedral shapes (Fig. 1b), and through the deepening and widening of step edges along cleavage planes (Fig. 1c). Etch pit steps were typically one unit cell (4.72 Å) high, before deepening. A high nucleation rate of small etch pits over the reactive surface was observed and these pits spread sideways to merge and remove successive unit-cell heights layer by layer. The dissolution rate v_{diss_pit} was measured from etch pit

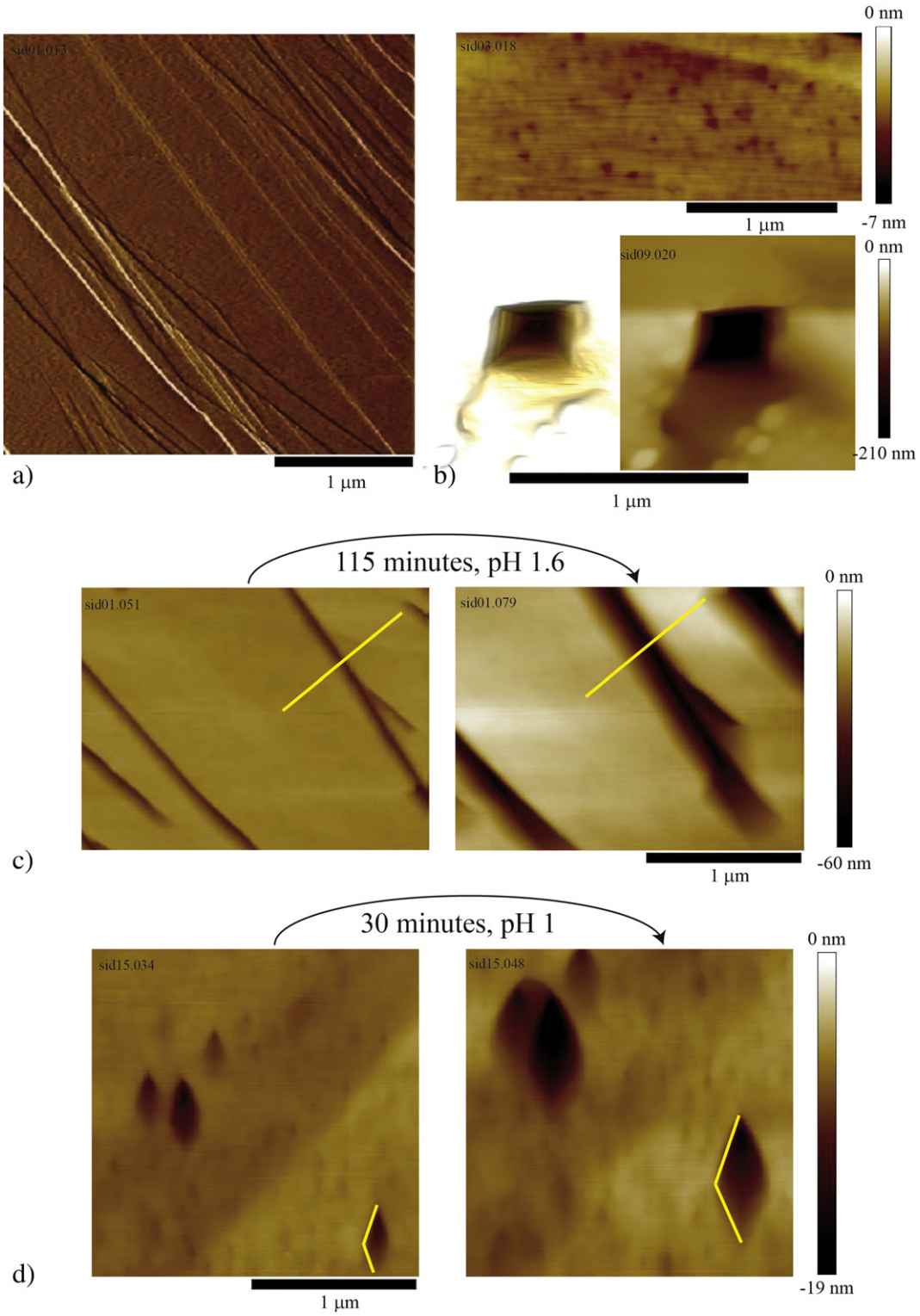

Fig. 1. In-situ AFM images of a siderite surface. a) Dry cleaved surface showing steps (image in deflection mode). Siderite steps are mostly one unit cell, 4.72 Å high. b) Rhombohedral etch pits forming on the siderite surface during dissolution in a flow-through fluid cell. Top (height mode): one unit cell deep etch pits start developing. Bottom (3D view, left, and height mode right): 210 nm deep 4-sided etch pit. c) Dissolution occurs also by widening and deepening of cleavage steps (exp. sid09, $As^{(V)}$ 500 ppm, pH 2.1, see Table 1). The yellow line corresponds to the time-lapse height profiles shown on Fig. 2. d) Dissolution along etch pits and etch pit merging. The dissolution rate can be measured through the length increase of etch pit sides (yellow lines).

spreading (see Ruiz-Agudo and Putnis (2012) for details of measurements and etch pit growth in Fig. 1d). Some deeper pits also formed as rows along the surface, probably indicating the position of defects or ion substitutions. Dissolution along steps of cleavage directions was also frequently observed. In one case, the direct dissolution rate could be measured as the dissolution along a cleavage step was followed for 115 min (see profile in Fig. 1c). The widening and deepening of the step was characterized (Fig. 2) and showed non-linear time evolution. Note that the ratio between width and depth of the steps remained constant (linear trend in Fig. 2d), indicating that dissolution occurred by the

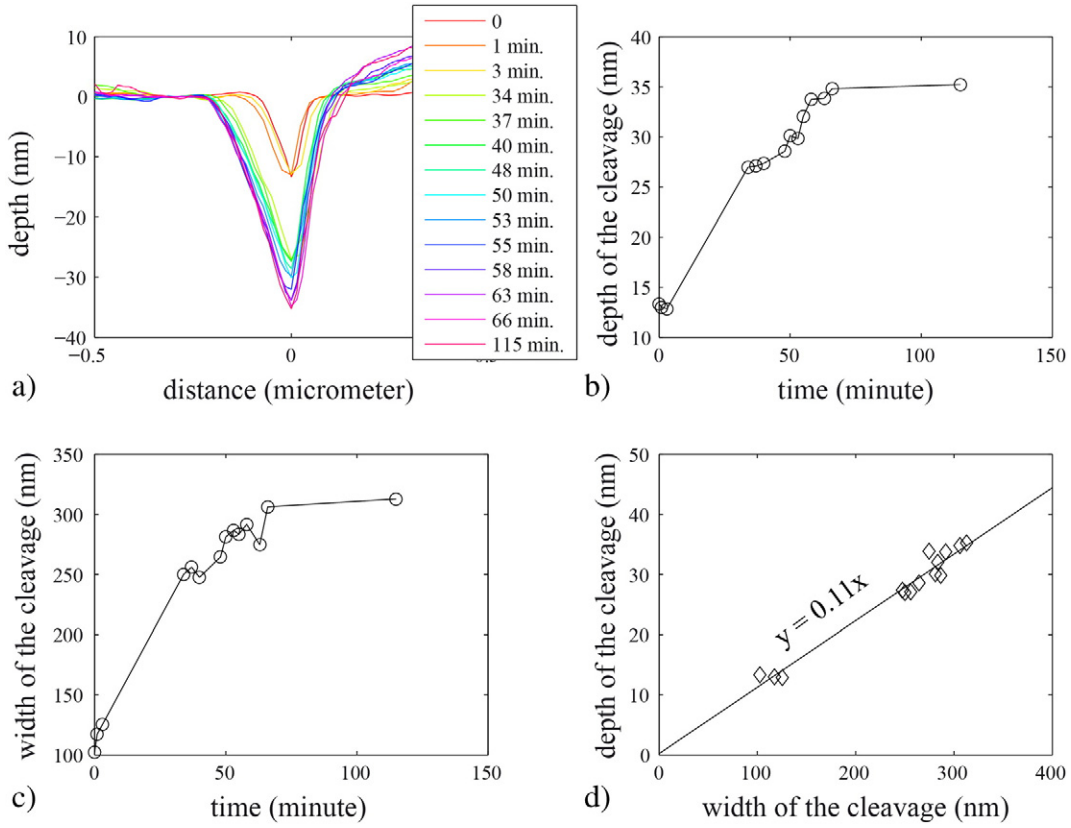

Fig. 2. Dissolution along a siderite surface (exp. sid09, $As^{(V)}$ 500 ppm, pH 2.1, see Table 1), where a cleavage step deepens and widens with time. a) Time-lapse profiles perpendicular to the cleaved (10–14) surface (the profile is shown on Fig. 1c). b) Depth as a function of time. c) Width as a function of time. d) Depth as a function of width showing a linear relationship and indicating dissolution perpendicular to the interface that preserves the wedge geometry of the cleavage.

removal of the constituent ionic species perpendicular to the surface. The rate of siderite dissolution normal to the surface (Fig. 2a), was measured equal to $v_{diss\_cleav} = 0.005 \pm 0.002$ nm·s^{-1}, for this example where pH was 2.1 and temperature was 23 °C. Taking the molar volume V_m of siderite into account (29.43 cm^3·mol^{-1}), a local kinetics constant can be calculated as $k_{loc} = v_{diss\_cleav}/V_m$ and is in the range $1.7 \times 10^{-7} \pm 0.7 \times 10^{-8}$ mol·m^{-2}·s^{-1}, and $\log_{10}(k_{loc}) = -6.8$. This value is very close to the value $\log_{10}(k) = -6.5$ measured by Duckworth and Martin (2004) using batch reactor experiments and representing a dissolution rate averaged over a large number of grains. At pH 1, the rate of etch pit propagation could be measured (Fig. 1d) and found to be $v_{diss\_pit} = 0.14 \pm 0.05$ nm·s^{-1}. This dissolution was very localized, therefore an average dissolution rate could be calculated only if the density of these etch pits over the whole surface of the sample could have been estimated, which is not the case here.

The precipitates initially formed as small spots, with an average size of a few nanometers (Fig. 3a, b), distributed more or less randomly on the siderite surface and showed low adhesion, as they were easily moved by the AFM tip at the initial stage of precipitation. With time, they tend to localize near step edges (Fig. 3c) or near deep etch pits (Fig. 3d) or, close to locations where dissolution was more intense. This means that dissolution sites, where more iron was released, control the nucleation process of ferric precipitates. Then, these precipitates grew in size into larger rounded structured aggregates, probably growing by an aggregation process, as already observed using high resolution TEM and X-ray microscopy imaging of several iron oxyhydroxides produced in micro-reactors (Abou-Hassan et al., 2009; Byelov et al., 2013), see Fig. 3e. After leaving the sample overnight, these precipitates covered the entire surface of the siderite (Fig. 3f) and showed preferential alignment along steps.

The shape and size of these precipitates can be measured in all experiments where they were observed (Fig. 4) and all showed that they formed patches with a more or less circular perimeter, a low height to diameter aspect ratio, and no evidence of crystallographic facets. Images were collected at different times, under different conditions, and over differing areas of observation. Also scanning was performed in different directions. Under all these conditions the precipitated particles we observed presented rounded perimeters. At the scale of our AFM observations tip-shaped convolutions would therefore be minimal and we conclude that the circular shapes measured are representative of the precipitate particles.

The diameter of the precipitates measured for one experiment at pH 2.1 at three different times (0.1, 1, 23 h) show mean values in the range 130–220 nm with standard deviation of ±60 nm (Fig. 4b). This quite large standard deviation does not allow us to determine whether the average precipitate diameter increases or decreases with time, and on average, within the deviation, it appears to remain constant. The heights of the precipitate particles tend to increase with time (Fig. 4c), reaching up to 80 nm after 24 h. The trend for the height increase with time is robust with a constant linear growth velocity of 0.012 nm/s (Fig. 4d), higher than the values in the range 0.0001–0.0006 nm/s measured by Weidler et al. (1998) for the growth of goethite, at pH close to 5 and probably different supersaturation, however.

To summarize, the coupled dissolution-precipitation process involves the dissolution of the siderite substrate, releasing $Fe^{(II)}$, and the nucleation of precipitates that grew in diameter until they reached a size in the range 130–220 nm, and then grew in height to 10–80 nm. With time the siderite surface became covered by these particles that produced several layers of precipitates (Fig. 3f). There is therefore a balance between nucleation of new precipitates and growth of existing ones. Their rounded shape probably indicates low crystallinity or possibly an amorphous phase. These observations are seen for very acidic to low acidic fluids, whether or not arsenic is present. For the two experiments at high pH (experiments sid13 and sid14 in Table 1), no evidence

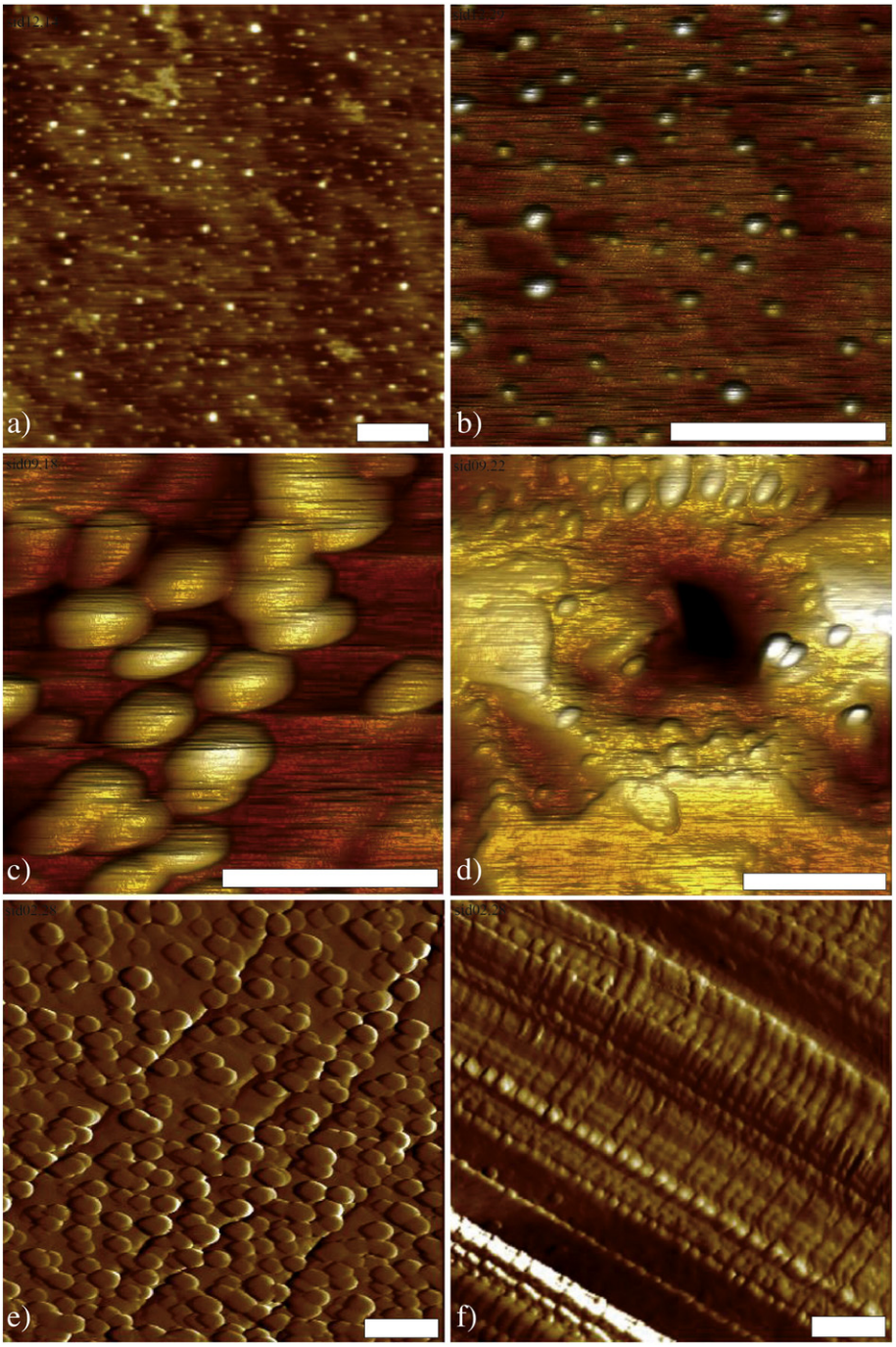

Fig. 3. AFM images of iron oxide/hydroxide precipitates on a siderite surface. Scale bar: 500 nm for all images. a–b) Small iron oxyhydroxide particles randomly precipitated on the siderite surface (height mode, exp. sid12, no arsenic, pH 2.8, see Table 1); c–d) Iron oxyhydroxide precipitates, with an etch pit showing evidence of dissolution (d) coupled to precipitation (height mode, exp. sid09, $As^{(V)}$ 500 ppm, pH 2.1, see Table 1). e–f) Iron oxide/hydroxide particles aligned along steps of the siderite surface (deflection mode, exp. sid02, $As^{(V)}$ 500 ppm, pH 1.6, see Table 1).

of dissolution was observed and no precipitates could be observed, probably because the kinetics was slower and could not be captured during the course of an AFM experiment (averaging several hours).

The surface dissolution-precipitation reactions, including iron oxidation at the siderite surface can be written as follows:

$$\equiv FeCO_3 + H^+ \rightarrow Fe^{(2+)} + HCO_3^- \quad (\text{dissolutionprocess})$$

$$Fe^{(2+)} + HCO_3^- + 0.5O_2 + 1e \rightarrow FeOOH + CO_2 \quad (\text{ironoxidation and oxyhydroxideprecipitation})$$

Here, we assume the most common iron oxyhydroxide group (goethite, lepidocrocite, and akaganeite) in oxidant systems.

3.2. Ex-situ experiments

The stirred flow-through reactor experiments (see Section 2.4) showed an initial increase of iron concentration in the fluid collected at the outlet, and demonstrated siderite dissolution (Fig. 5). After about 100 min, the concentration of iron in the fluid tends to decrease, which is interpreted by the precipitation of iron oxyhydroxides. Despite the high amount of arsenic used in these experiments, no clear

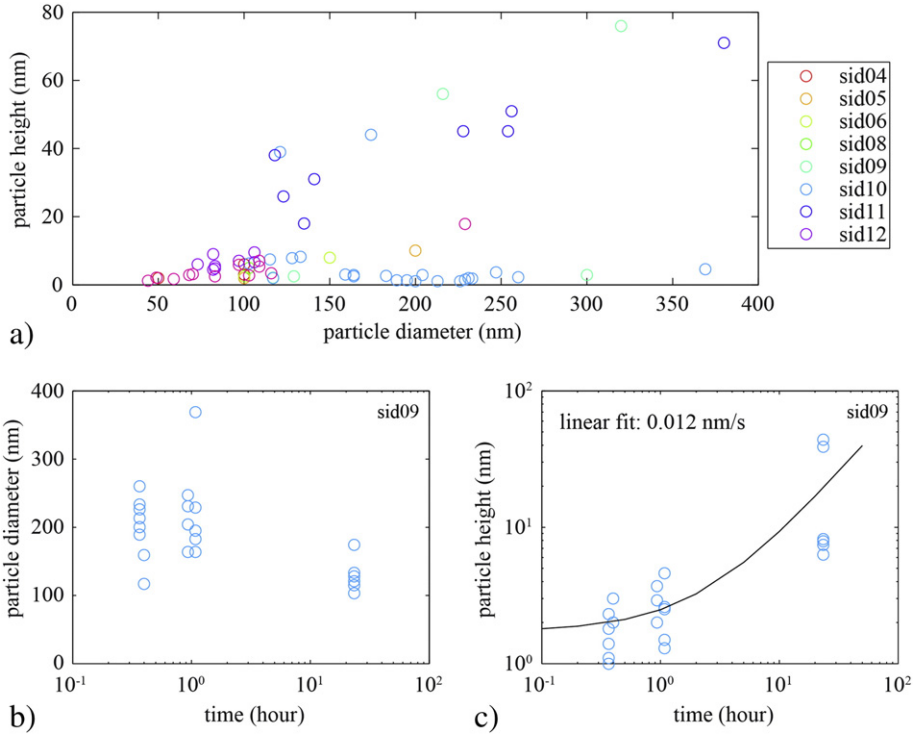

Fig. 4. Analysis of the shape of the iron oxyhydroxide particles precipitated on siderite surfaces. a) Particle height versus diameter. b–c) For experiment sid09 ($As^{(V)}$ 500 ppm, pH 2.1, see Table 1), the evolution of the particle diameter (c) and height (d) as a function of time is shown. The average particle diameter does not change significantly with time whereas the height of iron oxyhydroxide particle tends to increase with time (best linear fit is given).

adsorption could be observed. This is due to the fact that arsenic adsorbs more preferentially on iron oxyhydroxide rather than onto siderite and the rate of iron oxyhydroxide production was slow when considering the experimental durations used here. Scanning electron microscopy images showed the precipitation of iron oxyhydroxide on siderite (Fig. 5f). The stirred-flow reactor experiments therefore confirm what was observed in-situ by AFM, that is, a coupled dissolution-precipitation process where the iron produced by siderite dissolution was oxidized forming particles of iron oxyhydroxide precipitates.

3.3. Raman measurements

Coupled to dissolution, precipitates formed on the siderite surface (Fig. 3). The precipitated particles were generally too small and reacted with the Raman laser beam thus making them difficult to analyze using Raman spectroscopy. After experiments in the flow-through reactor, the solid reaction product was also analyzed using Raman spectroscopy (Fig. 6).

A broad Raman peak was observed at 857 cm^{-1} after the reactor experiments at pH 5 (spectrum D in Fig. 6). This is consistent in position with the observed double peak produced during arsenic adsorption to amorphous Fe-oxides in pH 5 solutions (Goldberg and Johnston, 2001). A slight shoulder is also observed at lower wavenumbers on the siderite related peak at ~730 cm^{-1} indicating the presence of an iron-phase such as ferrihydrite, which produces a weak broad band in this region (Hanesch, 2009). A weak broad peak in the same position was also observed after the pH 2 reactor experiments along with a second phase that produced more intense peaks at 244, 370, 640 cm^{-1}. This is similar to goethite, although at lower wavenumbers than those reported previously (Hanesch, 2009). In addition, the spectra indicate that a hydrated Fe-arsenate phase forms in these experiments.

The AFM experiment sid10 (pH 5.5, no arsenic, see Table 1) showed precipitates with peaks at 242, 393 and 637 cm^{-1}. The orange colour of the precipitates visible under the light microscope of the Raman spectrometer and the similarity of the peak positions to other Fe-oxyhydroxide phases (Hanesch, 2009) as well as the expected formation of akaganeite and goethite under the experimental conditions, indicates that the precipitates are probably an iron-oxyhydroxide phase. To conclude, both SEM imaging coupled to EDS (Fig. 5f) and Raman spectroscopy (Fig. 6) performed on flow-through reaction products and one sample used for AFM experiments indicate that the precipitates are oxyhydroxides (goethite, ferrihydrite). In some cases, the existence of an As-Fe phase is detected by a weak Raman peak (spectrum D in Fig. 6). However, it cannot be a major phase in the system studied here.

4. Discussion

In the experiments, the pH of the injection solution is fixed whereas the Eh potential is not controlled. In both AFM flow cell and flow-through reactors, the injected fluid is in equilibrium with atmospheric oxygen, and the conditions are oxic. If one considers the pH/Eh diagram of iron in water (Beverskog and Puigdomenech, 1996), the experimental conditions are near the end of the stability field for $Fe(OH)_3$ where high quite Eh is needed to precipitate oxyhydroxide. Further, if one overlaps the Eh/pH stability field of arsenic (Lu and Zhu, 2011) on top of the Fe-H_2O system diagram, arsenic is soluble in the experimental conditions. These two Eh/pH diagrams are represented on the Fig. 7. The experiments were likely saturated by atmospheric oxygen, but given the isolated set-up of AFM fluid cell, there is a possibility that the Eh could drop quickly when siderite dissolves to release ferrous ion. In this case, arsenic adsorption will be less significant. However, in cases where iron oxyhydroxide precipitates are widespread, arsenic can adsorb on these phases and be removed from the solution.

4.1. Dissolution of siderite

Carbonate minerals dissolve with a rate that decreases from calcite to dolomite, siderite, and magnesite. The dissolution reaction of siderite

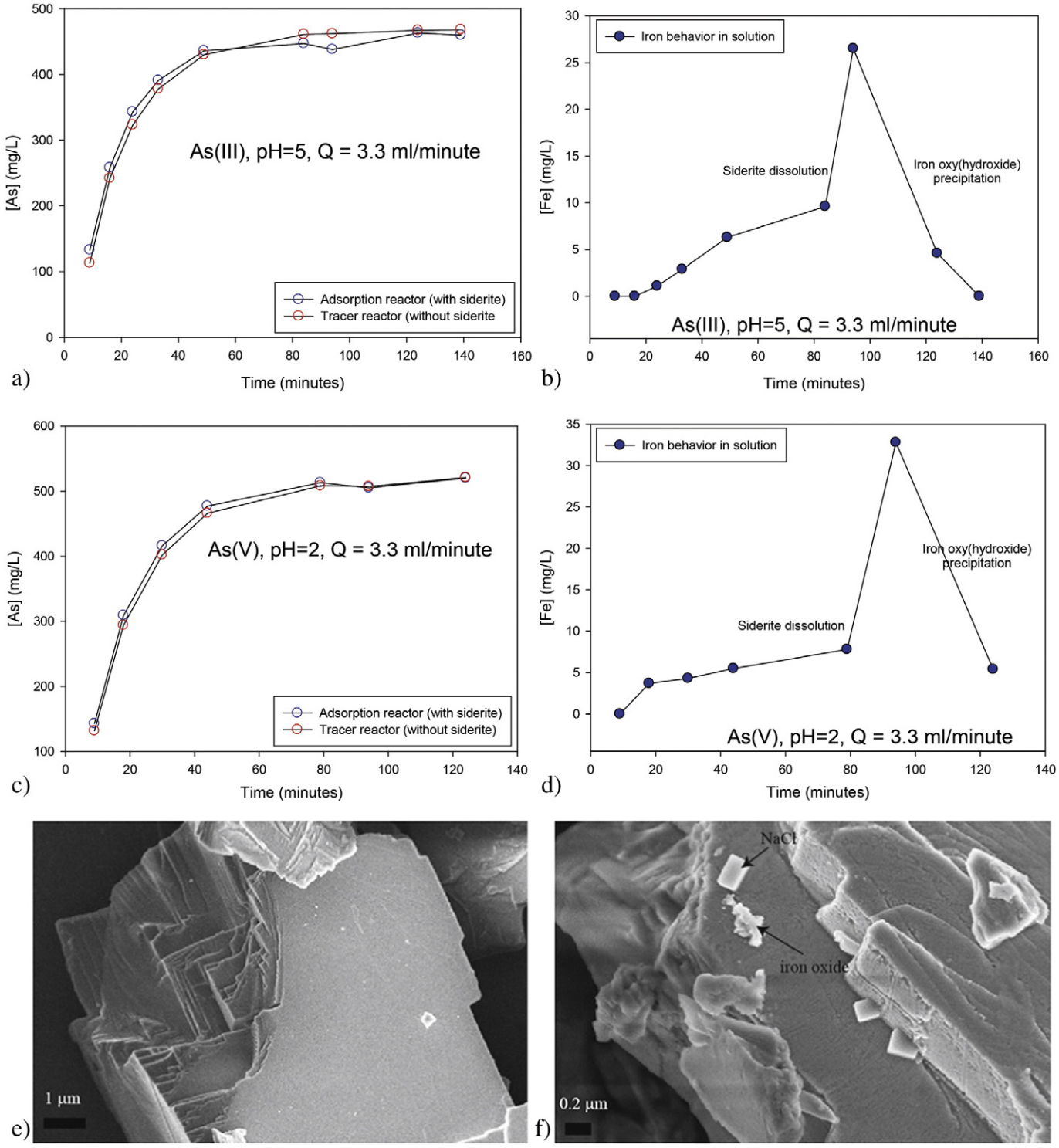

Fig. 5. Results of stirred flow-through reactor experiments and field emission scanning electron microscopy image of siderite crystals and precipitates of iron oxyhydroxide. a–b) Siderite at pH 5 with $As^{(III)}$ 500 ppm (exp. Ba1, see Table 1): no adsorption of As could be detected (a), whereas the time evolution of iron concentration in the fluid shows an initial increase (siderite dissolution) and a drop after around 100 min (iron oxyhydroxide precipitation). c–d) Same as a–b) for a solution at pH 2 and $As^{(V)}$ 500 ppm (exp. Ba2, see Table 1). e–f) Field emission scanning electron microscopy image of an unreacted siderite grain used for the stirred flow-through reactor experiments (e) and siderite grain after reaction showing small iron oxyhydroxide precipitates and NaCl crystals (f). NaCl is an evaporation product after the conclusion of the experiments.

under conditions relevant for natural environments, such as bottoms of lakes or geological reservoirs, was measured in several studies (Singer and Stumm, 1970; Reiterer et al., 1981; Bruno et al., 1992; Duckworth and Martin, 2004; Tang and Martin, 2011). Siderite dissolves in water according to the reaction $FeCO_{3(s)} + 2H^+ \rightarrow H_2O + CO_{2(g)} + Fe^{2+}$, with an equilibrium constant K_0 equal to $10^{-7.59}$ at 25 °C, under neutral pH conditions and in a 1 M $NaClO_4$ solution (Bruno et al., 1992). At pH below 6.5, room temperature, and in the absence of oxygen, the iron remains in the form of dissolved Fe^{2+} in the fluid, whereas at pH above this limit, ligands form in the fluid such as $FeCO_{3(aq)}$ up to pH 8.5 and $Fe(CO_3)_2^{2-}$ above 8.5 (Bruno et al., 1992). The kinetics of dissolution at 25 °C and in oxic and anoxic conditions is constant at pH in the range 5.5–10 and increases by decreasing the pH below 5.5 (Duckworth and Martin, 2004).

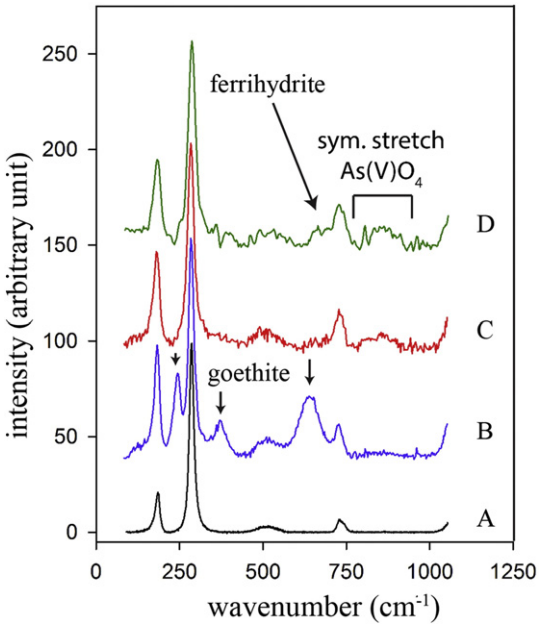

Fig. 6. Raman spectra showing original siderite (black, A), precipitates from the pH 2 flow-through reactor experiment without (blue, B) and with (red, C) the peak at 857 cm^{-1} characteristic of arsenate symmetrical stretching vibration and precipitate from the reactor experiment at pH 5 (green, D). Peaks of goethite are clearly visible in sample B (black arrows), and a weak peak at the position of ferrihydrite could also be observed on sample D.

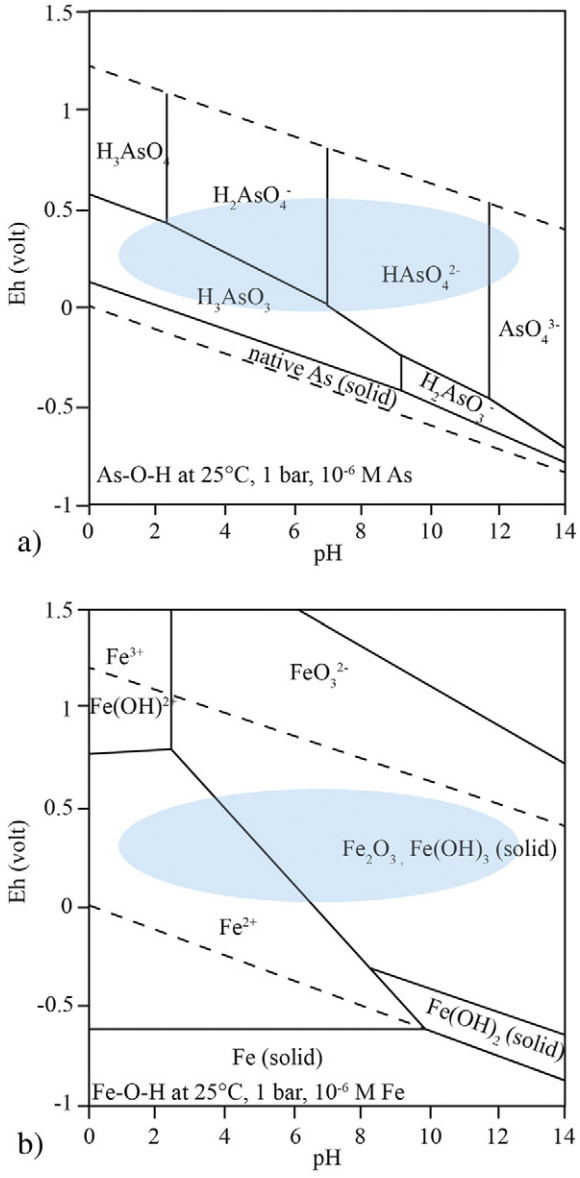

Fig. 7. Pourbaix diagrams for a) iron (Beverskog and Puigdomenech, 1996) and b) arsenic (Lu and Zhu, 2011) at 25 °C and 1 bar in the water system. The conditions of the AFM and flow-through reactor experiments are underlined by the shaded ellipse.

Atomic force microscopy images show that dissolution occurs by the formation and extension of rhombohedral etch pits, sometimes aligned along cleavage or fracture planes, and retreating of step edges (Duckworth and Martin, 2004; Tang and Martin, 2011). This is consistent with other carbonate mineral dissolution (see Ruiz-Agudo and Putnis (2012) for a review of AFM measurements and observations). Duckworth and Martin (2004) observed that the shape of rhombohedral etch pits with an initial obtuse angle of 102° evolved during dissolution and the obtuse angle decreased to 72° after 4 h. Tang and Martin (2011) observed alignments of etch pits along fractures and dissolution by step edge retreat. Here, we show that a complementary mechanism, the widening and deepening of cleavage steps is also involved in siderite dissolution. When observing the dissolution of cleavage steps in AFM, their widening gives access to the rate in a plane perpendicular to the dissolving interface, whereas etch pits are usually interpreted as showing the rate of dissolution of atoms in the plane of the interface. Our data show that dissolution occurs at the mineral-water interface in-plane (by etch pit lateral propagation) and in a perpendicular direction (by etch pit deepening or dissolution at cleavage steps). Moreover, we provide dissolution rates at the microscopic scale, $v_{diss\_pit} = 0.14 \pm 0.05$ $nm \cdot s^{-1}$ for the spreading of etch pits at pH 1 and $v_{diss\_cleav} = 0.005 \pm 0.002$ $nm \cdot s^{-1}$ for the widening of cleavage at pH 2.1.

Golubev et al. (2009) studied the kinetics of siderite dissolution in batch reactor experiments, at pH in the range 1 to 4.6 and partial pressure of CO_2 in the range 10^5–$5 \cdot 10^6$ Pa. They showed that the siderite dissolution rate decreases with increasing pH in the range 1–4.5, and increases with temperature with an activation energy in the range 48–61 $kJ \cdot mol^{-1}$, depending on pH and a negligible effect of the partial pressure of CO_2. The dissolution rate of siderite was measured on powder at 25 °C close to $10^{-6.5}$ $mol \cdot m^{-2} \cdot s^{-1}$ at pH 1.5 and decreases to $10^{-8.65}$ $mol \cdot m^{-2} \cdot s^{-1}$ as pH increases to 6, as seen in the Fig. 2 in Duckworth and Martin (2004). A slightly higher value was obtained by Golubev et al. (2009) when using a rotating disk apparatus, with a dissolution rate decreasing from $10^{-5.2}$ to 10^{-6} $mol \cdot m^{-2} \cdot s^{-1}$ while the pH increases from 1 to 3. A value of $10^{-6.5}$ $mol \cdot m^{-2} \cdot s^{-1}$ at pH 2 was obtained by Tang and Martin (2011), which then decreases as pH increases. All these values measured with different techniques and by different groups point to the same value, similar to what we measured on the lateral widening of a cleavage step (Fig. 2) and indicating that the dissolution rate at a local scale is similar to that of the bulk.

4.2. Iron oxyhydroxide precipitation in a boundary solution layer

The dissolution of siderite may be more complex because it is coupled to the precipitation of iron oxyhydroxides that would then tend to passivate siderite surfaces, reducing dissolution. At pH below 10.3, a mechanism of coupled dissolution and precipitation has been proposed that involves four successive steps: 1) the release of Fe^{2+} by siderite dissolution, 2) the formation of a $(Fe^{2+}OH)^+$ complex that reacts with O_2 present in the fluid, 3) the formation of an aqueous complex $(Fe^{3+}(OH^-)_3)^0$, and 4) the precipitation of solid $Fe^{III}(OH)_3$ (Duckworth and Martin, 2004; Tang and Martin, 2011). The precipitation of an $Fe^{(III)}$ oxyhydroxide layer may cover the siderite surface (Guo et al., 2007a; Tang and Martin, 2011), passivate it, and significantly modify dissolution rates. We directly observe this effect during in-situ

experiments where iron oxyhydroxides precipitate on the siderite surface and cover it in <24 h for the low pH solutions. Here, we show as well that the oxyhydroxides nucleate or arrive at the surface as tiny nm size particles and then initially grow as probably non-crystalline rounded (amorphous) particles, 130–250 nm wide and up to 80 nm height. They accumulate on the siderite surface and could produce several successive layers, decreasing the surface area available for further dissolution.

Davison and Seed (1983) measured the kinetics of oxidation of $Fe^{(II)}$ into $Fe^{(III)}$ in natural freshwaters and the laboratory in the neutral pH range and fitted the following kinetic relationship:

$$-\frac{d\left[Fe^{(II)}\right]}{dt} = k\left[Fe^{(II)}\right]pO_2[OH^-]^2 = k_1\left[Fe^{(II)}\right]$$

where k is the rate constant, pO_2 is the partial pressure of oxygen, $[OH^-]$ represents the effect of pH, and k_1 is a rate constant where the effects of oxygen and pH are embedded together. At room temperature, partial pressure of oxygen close to atmospheric and pH close to neutral, the value of k is close to $2\cdot10^{13}$ $mol^{-2}\cdot L^2\cdot atm^{-1}\cdot min^{-1}$ and the half time of the reaction is in the range 1–6 h. Applied to the present experiments, the time scale of $Fe^{(II)}$ oxidation is therefore larger than the time scale of the whole dissolution-precipitation process we observe. This implies that the oxidation of $Fe^{(II)}$ could be the limiting step of the whole dissolution-precipitation process. It also implies that because the time scale for the whole process measured in the AFM experiments is shorter than what Davison and Seed (1983) measured for the oxidation of $Fe^{(II)}$, either the access of oxygen in our experiments is easier than in their experiments, or the presence of siderite and/or goethite helps to catalyze this oxidation reaction, as already proposed in other studies (Weidler et al., 1998; Liu et al., 2007).

The growth of goethite crystals was studied using atomic force microscopy at room temperature and pH 4.85 (Weidler et al., 1998). Results show that (100) and (110) faces of goethite grow at velocities in the range $1–6\times10^{-4}$ $nm\cdot s^{-1}$, which is one to two orders of magnitude slower than what we measured in our AFM experiments for the growth in height of the oxyhydroxide particles at pH 2.1 (Fig. 4d). The difference between the rate they measured at pH 4.85 and the rate measured in the present study at pH 2.1 could be related to the fact that dissolution of siderite is two orders of magnitude faster at pH 2.1 than at pH 4.85, releasing much more iron in solution, and increasing the local supersaturation with respect to goethite near the surface. Weidler et al. (1998) calculated that the rate of $Fe^{(III)}$ complexation at the goethite surface was one to two orders of magnitude larger than in the bulk solution, and that therefore goethite catalyzed this transformation. In addition, the presence of trace amount of $Fe^{(II)}$ adsorbed on ferrihydrite can catalyze its transformation into goethite, even at room temperature (Liu et al., 2007).

Two models for precipitation of iron oxides can be proposed: 1) the homogeneous nucleation in the fluid by oxidation of $Fe^{(II)}$, or 2) the heterogeneous nucleation at siderite or iron oxyhydroxide surfaces. Our data show that the iron oxyhydroxides precipitate directly on the siderite surface, favoring the heterogeneous nucleation model. As mentioned previously, the nucleated nanoparticles grew by aggregation of primary nanoparticles, then leading to rounded structured aggregates similar to mesocrystals if crystalline nanoparticles are involved (Montes-Hernandez et al., 2015); however, from AFM observations it is difficult to obtain information on the crystallinity of precipitating particles. The subsequent coalescence of nanometer size particles to form larger single crystals has been reported for the growth of both calcite and barite (Gebauer et al., 2008; Ruiz-Agudo et al., 2015) and has contributed to the current debate about non-classical crystal growth mechanisms (Teng, 2013).

From the AFM observations, the first particles (a few nm in size) were present on the siderite surface immediately within the first second of scanning and appeared to come directly from solution as opposed to nucleating on the surface. Then after successive scans (each scan lasted 65–70 s) the small nanometer sized particles could be seen to increase in size by coalescence with adjacent particles (Fig. 3e–f).

The solubility product $K_{S,O}$ of $Fe^{(III)}$ oxyhydroxide equilibrium in aqueous solution follows the relationship $K_{(s,o)} = a_{(Fe(III))}(a_{OH^-})^3$ at 25 °C and shows cubic pH dependence. The value of $K_{s,o}$ is $10^{-41.8}$ for goethite and 10^{-39} for ferrihydrite (see Table VII-13, p. 228 in Lemire et al., 2013; Stefánsson, 2007). This indicates that goethite has a slightly lower solubility compared to ferrihydrite, and therefore should precipitate first if the kinetic rate allows it. Applied to the experiment sid02 (pH 1.6, 500 ppm $As^{(V)}$, see Table 1), the concentration of $Fe^{(III)}$ next to the siderite surface is high enough to precipitate goethite. This implies that locally the solubility of $Fe^{(III)}$ is above the equilibrium value at this pH, $K = 2.5\times10^{-2}$ $mol\cdot m^{-3}$. Under these conditions, the rate of siderite dissolution measured from the AFM experiments is of the order of $R = 10^{-7}$ $mol\cdot m^{-2}\cdot s^{-1}$ (see Section 3.1). We now consider a simplified system where $Fe^{(III)}$ is produced at a rate R above the siderite surface and diffuses perpendicular to it with a length scale $L_{diff} = \sqrt{Dt}$, where D is the diffusion coefficient of water, of the order of 2×10^{-9} $m^2\cdot s^{-1}$, and t is time. Then, one can define the characteristic thickness $L_b = \frac{KD}{R}$ of a thin boundary layer in which the iron concentration is higher than K in our experiments. Using the values given above for K, D, and R, one obtains $L_b = 250$ μm. This simple scaling relationship indicates that the fluid above siderite can remain supersaturated with respect to iron at distance orders of magnitude larger than the height of the oxyhydroxide precipitates observed to form, as long as siderite continues to dissolve. In this boundary layer, the pH will be buffered by the release of carbonate groups from the siderite that will increase locally the pH and therefore will reduce the value of K, increasing even more the supersaturation with respect to goethite. Such variations of fluid pH at mineral surfaces during dissolution have been reported using phase-shift interferometry (Ruiz-Agudo et al., 2016).

A more complex model would take into account the rate of $Fe^{(II)}$ oxidation, the rate of precipitation of iron oxyhydroxides, the speciation of iron species, and the buffering of pH in the boundary layer, but would not change the conclusion that a thin layer with specific thermodynamic properties is present above the siderite crystal and act as a micro-reactor for the precipitation of iron oxyhydroxide particles. Another implication is that this local increase of pH would favor adsorption of arsenic onto the newly formed iron oxyhydroxide particles.

We also observed that, after some time, oxyhydroxide particles were attached to the surface and were not removed by the AFM tip during the scanning. They must have had some form of bonding at the surface and therefore the underlying siderite structure must have been involved in that attachment, in addition to the boundary layer effect.

To summarize, there is a clear control of the siderite surface on the precipitation of iron oxyhydroxide particles. This control is mainly due to the presence of a fluid boundary layer where iron will be more concentrated in the fluid near the siderite surface, and where the dissolution rate exceeds diffusion of ionic species away from the dissolving surface. This is similar to observations reported for the precipitation of arsenic or selenium phases on calcite (Putnis et al., 2013; Renard et al., 2015).

4.3. Adsorption of arsenic

The interactions of arsenic with minerals and solutions represent an important environmental issue, and several natural systems show both high arsenic concentration and low fluid pH, such as acid mine or borehole fluid drainage (Benner et al., 1999; Nordstrom et al., 2000) and remediation is a key challenge (Mohan and Pittman, 2007). We discuss here how arsenic interacts with siderite and iron oxyhydroxides in our experiments. The two main observations are that 1) arsenic adsorbs mainly on iron oxyhydroxides and a little, if any, on siderite, 2) the presence of high arsenic concentration in the fluid does not significantly

modify the mechanism nor the rate of the coupled dissolution-precipitation process.

Jönsson and Sherman (2008) have studied the sorption of arsenic on synthetic iron carbonates and found that at pH above 7, siderite strongly adsorbs arsenic, whereas at lower pH, it was not possible to measure this adsorption due to the production of iron oxides. Conversely, the adsorption capacity of iron oxides can reach 20 mg of arsenic adsorbed per gram of dry iron oxide, with values usually <5 mg/g in most sets of laboratory experiments (Badruzzaman et al., 2004; Westerhoff et al., 2005; Mohan and Pittman, 2007).

The strong adsorption of arsenic in various oxidation states ($As^{(III)}$ and $As^{(V)}$) on iron oxides, such as amorphous goethite and magnetite, has been measured by Dixit and Hering (2003) in solutions in a range of pH between 4 and 10. The amount of adsorbed arsenate ($As^{(V)}$) and arsenite ($As^{(III)}$) on ferrihydrite varies slightly with pH in the range 3–11, with trends of increasing adsorption for arsenite and decreasing adsorption for arsenate as pH increases in the range 2.5–9 (Raven et al., 1998; Dixit and Hering, 2003). Above pH ~ 9, arsenite adsorption on iron oxyhydroxide decreases as well (see Fig. 7 in Raven et al., 1998).

Arsenate tetrahedra adsorb onto ferrihydrite iron oxides by linking an edge with Fe octahedra, based on EXAFS measurements of the distance between $Fe^{(III)}$ and $As^{(V)}$ atoms (Manceau, 1995). This adsorption also retards the growth of iron particles and slows down the rate of transformation of ferrihydrite to hematite. It is controlled by the surface charge and density of sorption sites on iron oxides that both vary with pH and fluid composition (Goldberg and Johnston, 2001; Dixit and Hering, 2003).

In our experiments we observe that the presence of arsenic does not significantly change the mechanism of siderite dissolution, nor the precipitation of iron oxyhydroxides: the pattern of dissolution and the morphology of precipitates is independent of the presence or absence of arsenic. When iron oxyhydroxides precipitate, however, the adsorption of arsenic onto these minerals is expected, as has been demonstrated in a previous study (Dixit and Hering, 2003). Our situ observations indicate that the continuous production of iron oxyhydroxide due to the dissolution of siderite will create new adsorption sites for arsenic on the one hand, but on the other hand these particles of oxyhydroxides cover the surface of siderite and may passivate it in less than a day at pH below 2.

5. Conclusion

The coupled process of siderite dissolution in acidic aqueous fluids, in the presence of arsenic, was studied in-situ using atomic force microscopy (Fig. 8). The main results are:

- Dissolution of siderite occurs by the nucleation of etch pits and step edge retreat, as observed previously (Duckworth and Martin, 2004; Tang and Martin, 2011), and by a third mechanism identified here, the widening and deepening of cleavage planes.
- Coupled to siderite dissolution, iron oxyhydroxide precipitates as nanometer size particles on the surface (heterogeneous nucleation) and primary nanoparticles are then self-assembled into rounded aggregates that coalesce to form larger particle aggregates, probably amorphous, 130–220 nm wide and up to 80 nm high that cover the carbonate surface. This process reduces the surface area available for dissolution and may passivate the siderite surface. Goethite and a weak Raman peak at the position of ferrihydrite were identified from flow-through reactor experiments.
- The presence of arsenic, even at high concentration, does not significantly modify the siderite dissolution process. Arsenic preferentially adsorbs onto the iron oxyhydroxide precipitates formed from the interface-coupled dissolution and precipitation process occurring under acidic aqueous conditions, typically occurring in acid mine drainage environments.

Acknowledgements

The authors thank V. Rapelius for help with ICP-OES analyses at Münster University and Sarah Bureau for the help with ICP-AES analyses at Univ. Grenoble Alpes. The experimental facilities in the Institut für Mineralogie, University of Münster, are supported by the German Research Council (DFG). Funding from Labex OSUG@2020 (Investissement d'avenir-ANR10-LABX56) is acknowledged. This project has received funding from the European Union's Seventh Framework Program for

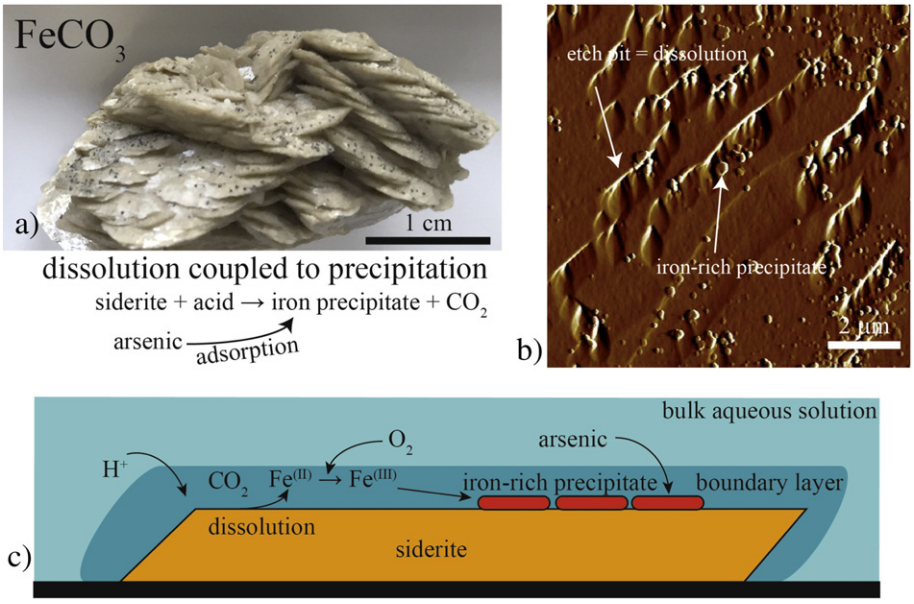

Fig. 8. Summary of the coupled process of siderite dissolution, iron oxyhydroxide precipitation, and arsenic adsorption. a) Natural siderite sample used for the AFM experiments. The sample was crushed and clean siderite millimeter-size and freshly cleaved crystals were used. b) AFM image of a siderite crystal surface in deflection mode, showing both etch pits (rhombohedral shapes) and iron oxyhydroxide precipitates (circular shapes). c) Sketch of the coupled dissolution-precipitation process.

research, technological development and demonstration through Marie Curie initial training networks Flowtrans (under grant agreement number 316889) and CO2React.

References

Abou-Hassan, A., Sandre, O., Neveu, S., Cubuil, V., 2009. Synthesis of goethite by separation of the nucleation and growth processes of ferrihydrite nanoparticles using microfluidics. Angew. Chem. 121, 2378–2381.

Badruzzaman, M., Westerhoff, P., Knappe, D.R., 2004. Intraparticle diffusion and adsorption of arsenate onto granular ferric hydroxide (GFH). Wat. Res. 38 (18), 4002–4012.

Benner, S.G., Blowes, D.W., Gould, W.D., Herbert, R.B., Ptacek, C.J., 1999. Geochemistry of a permeable reactive barrier for metals and acid mine drainage. Env. Sci. Tech. 33 (16), 2793–2799.

Beverskog, B., Puigdomenech, I., 1996. Revised Pourbaix diagrams for iron at 25–300 °C. Corros. Sci. 38 (12), 2121–2135.

Bruno, J., Wersin, P., Stumm, W., 1992. On the influence of carbonate in mineral dissolution: II. The solubility of $FeCO_3$ (s) at 25 °C and 1 atm total pressure. Geochim. Cosmochim. Acta 56 (3), 1149–1155.

Byelov, D.V., Meijer, J.-M., Snigireva, I., Snigirev, A., Rossi, L., van der Pol, E., Kuijk, A., Philipse, A., Imhof, A., van Blauderen, A., Vroege, G.J., Petukhov, A.V., 2013. In situ hard X-ray microscopy of self-assembly in colloidal suspensions. RSC Adv. 3, 15670–15677.

Chapman, E.C., Capo, R.C., Stewart, B.W., Hedin, R.S., Weaver, T.J., Edenborn, H.M., 2013. Strontium isotope quantification of siderite, brine and acid mine drainage contributions to abandoned gas well discharges in the Appalachian Plateau. Appl. Geochem. 31, 109–118.

Davison, W., Seed, G., 1983. The kinetics of the oxidation of ferrous iron in synthetic and natural waters. Geochim. Cosmochim. Acta 47 (1), 67–79.

Dixit, S., Hering, J.G., 2003. Comparison of arsenic (V) and arsenic (III) sorption onto iron oxide minerals: implications for arsenic mobility. Env. Sci. Tech. 37 (18), 4182–4189.

Duckworth, O.W., Martin, S.T., 2004. Role of molecular oxygen in the dissolution of siderite and rhodochrosite. Geochim. Cosmochim. Acta 68 (3), 607–621.

España, J.S., Pamo, E.L., Pastor, E.S., 2007. The oxidation of ferrous iron in acidic mine effluents from the Iberian Pyrite Belt (Odiel Basin, Huelva, Spain): field and laboratory rates. J. Geochem. Explor. 92 (2), 120–132.

Gebauer, D., Völkel, A., Cölfen, H., 2008. Stable prenucleation calcium carbonate clusters. Science 322 (5909), 1819–1822.

Goldberg, S., Johnston, C.T., 2001. Mechanisms of arsenic adsorption on amorphous oxides evaluated using macroscopic measurements, vibrational spectroscopy and surface complexation modelling. J. Colloid Interf. Sci. 234, 204–216.

Golubev, S.V., Bénézeth, P., Schott, J., Dandurand, J.L., Castillo, A., 2009. Siderite dissolution kinetics in acidic aqueous solutions from 25 to 100 °C and 0 to 50 atm pCO_2. Chem. Geol. 265 (1), 13–19.

Guo, H., Stüben, D., Berner, Z., 2007a. Adsorption of arsenic (III) and arsenic (V) from groundwater using natural siderite as the adsorbent. J. Colloid Interf. Sci. 315 (1), 47–53.

Guo, H., Stüben, D., Berner, Z., 2007b. Arsenic removal from water using natural iron mineral–quartz sand columns. Sci. Tot. Env. 377 (2), 142–151.

Hanesch, M., 2009. Raman spectroscopy of iron oxides and (oxy)hydroxides at low laser power and possible applications in environmental magnetic studies. Geophys. J. Int. 177, 941–948.

Hedin, R.S., Stafford, S.L., Weaver, T.J., 2005. Acid mine drainage flowing from abandoned gas wells. Mine Water Environ. 24 (2), 104–106.

Jönsson, J., Sherman, D.M., 2008. Sorption of As (III) and As (V) to siderite, green rust (fougerite) and magnetite: implications for arsenic release in anoxic groundwaters. Chem. Geol. 255 (1), 173–181.

Lemire, R.J., Berner, U., Musikas, C., Palmer, D.A., Taylor, P., Tochiyama, O., 2013. Chemical Thermodynamics of Iron, Part 1. NEA No. 6355. OECD. https://www.oecd-nea.org/dbtdb/pubs/6355-vol13a-iron.pdf.

Lin, Y.B., Lin, Y.P., Liu, C.W., Tan, Y.C., 2006. Mapping of spatial multi-scale sources of arsenic variation in groundwater on ChiaNan floodplain of Taiwan. Sci. Tot. Env. 370 (1), 168–181.

Liu, H., Li, P., Zhu, M., Wei, Y., Sun, Y., 2007. Fe (II)-induced transformation from ferrihydrite to lepidocrocite and goethite. J. Solid State Chem. 180 (7), 2121–2128.

Lu, P., Zhu, C., 2011. Arsenic Eh–pH diagrams at 25 °C and 1 bar. Environ. Earth Sci. 62 (8), 1673–1683.

Manceau, A., 1995. The mechanism of anion adsorption on iron oxides: evidence for the bonding of arsenate tetrahedra on free Fe (O, OH) 6 edges. Geochim. Cosmochim. Acta 59 (17), 3647–3653.

Milliken, K.L., 1998. Carbonate diagenesis in non-marine foreland sandstones at the western edge of the Alleghanian overthrust belt, southern Appalachians. Carbonate Cementation in Sandstones: Distribution Patterns and Geochemical Evolution, Special Publication 26 of the International Association of Sedimentologists, pp. 64–87.

Mohan, D., Pittman, C.U., 2007. Arsenic removal from water/wastewater using adsorbents—a critical review. J. Hazard. Mat. 142 (1), 1–53.

Montes-Hernandez, G., Renard, F., Findling, N., Auzende, A.-L., 2015. Formation of porous calcite mesocrystals from CO_2-H_2O-$Ca(OH)_2$ slurry in the presence of common domestic drinks. CrystEngComm 17, 5725–5733.

Morad, S., Ismail, H.B., Ros, L.D., Al-Aasm, I.S., Serrhini, N.E., 1994. Diagenesis and formation water chemistry of Triassic reservoir sandstones from southern Tunisia. Sedimentology 41 (6), 1253–1272.

Nordstrom, D.K., Alpers, C.N., Ptacek, C.J., Blowes, D.W., 2000. Negative pH and extremely acidic mine waters from Iron Mountain, California. Env. Sci. Tech. 34 (2), 254–258.

Pal, T., Mukherjee, P.K., Sengupta, S., Bhattacharyya, A.K., Shome, S., 2002. Arsenic pollution in groundwater of West Bengal, India - an insight into the problem by subsurface sediment analysis. Gondwana Res. 5 (2), 501–512.

Parkhurst, D.L., Appelo, C.A.J., 1999. Users guide to PHREEQC (version 2) A computer program for speciation, batch reaction, one dimensional transport and inverse geochemical calculations. Water-Resources Investigation report 99-4259. U.S. Geological Survey, Washington, DC, p. 312.

Putnis, C.V., Renard, F., King, H., Montes-Hernandez, G., Ruiz-Agudo, E., 2013. Sequestration of selenium on calcite surfaces revealed by nanoscale imaging. Env. Sci. Tech. 47, 13469–13476.

Raven, K.P., Jain, A., Loeppert, R.H., 1998. Arsenite and arsenate adsorption on ferrihydrite: kinetics, equilibrium, and adsorption envelopes. Env. Sci. Tech. 32 (3), 344–349.

Reiterer, F., Johannes, W., Gamsjäger, H., 1981. Semimicro determination of solubility constants: copper (II) carbonate and iron (II) carbonate. Microchim. Acta 75 (1–2), 63–72.

Renard, F., Putnis, C.V., Montes-Hernandez, G., Ruiz-Agudo, E., Hovelmann, J., Sarret, G., 2015. Interactions of arsenic with calcite surfaces revealed by in-situ nanoscale imaging. Geochim. Cosmochim. Acta 159, 61–79.

Rossi, C., Marfil, R., Ramseyer, K., Permanyer, A., 2001. Facies-related diagenesis and multiphase siderite cementation and dissolution in the reservoir sandstones of the Khatatba Formation, Egypt's Western Desert. J. Sed. Res. 71 (3), 459–472.

Ruiz-Agudo, E., Putnis, C.V., 2012. Direct observations of mineral-fluid reactions using atomic force microscopy: the specific example of calcite. Min. Mag. 76, 227–253.

Ruiz-Agudo, E., Kowacz, M., Putnis, C.V., Putnis, A., 2010. The role of background electrolytes on the kinetics and mechanism of calcite dissolution. Geochim. Cosmochim. Acta 74, 1256–1267.

Ruiz-Agudo, C., Ruiz-Agudo, E., Putnis, C.V., Putnis, A., 2015. Mechanistic principles of barite formation: from nanoparticles to micron-sized crystals. Cryst. Growth Des. 15 (8), 3724–3733.

Ruiz-Agudo, E., King, H.E., Patiño-López, L.D., Putnis, C.V., Geisler, T., Rodriguez-Navarro, C., Putnis, A., 2016. Control of silicate weathering by interface-coupled dissolution-precipitation processes at the mineral-solution interface. Geology 44 (7), 567–570.

Singer, P.C., Stumm, W., 1970. The solubility of ferrous iron in carbonate-bearing waters. J. Am. Water Works Assoc. 62 (3), 198–202.

Stefánsson, A., 2007. Iron (III) hydrolysis and solubility at 25 °C. Environ. Sci. Tech. 41 (17), 6117–6123.

Stel, H., 2009. Diagenetic crystallization and oxidation of siderite in red bed (Buntsandstein) sediments from the Central Iberian Chain. Spain. Sedim. Geol. 213 (3), 89–96.

Tang, Y., Martin, S.T., 2011. Siderite dissolution in the presence of chromate. Geochim. Cosmochim. Acta 75 (17), 4951–4962.

Teng, H.H., 2013. How ions and molecules organize to form crystals. Elements 9 (3), 189–194.

Walter, A.L., Frind, E.O., Blowes, D.W., Ptacek, C.J., Molson, J.W., 1994. Modeling of multicomponent reactive transport in g–roundwater: 1. Model development and evaluation. Water Resour. Res. 30 (11), 3137–3148.

Wang, Y., Reardon, E.J., 2001. A siderite/limestone reactor to remove arsenic and cadmium from wastewaters. Appl. Geochem. 16 (9), 1241–1249.

Weidler, P.G., Hug, S.J., Wetche, T.P., Hiemstra, T., 1998. Determination of growth rates of (100) and (110) faces of synthetic goethite by scanning force microscopy. Geochim. Cosmochim. Acta 62 (21), 3407–3412.

Westerhoff, P., Highfield, D., Badruzzaman, M., Yoon, Y., 2005. Rapid small-scale column tests for arsenate removal in iron oxide packed bed columns. J. Envir. Eng. 131 (2), 262–271.